


## Density wave states in the presence of an external magnetic field

Ian E. Powell and Sudip Chakravarty

Mani L. Bhaumik Institute for Theoretical Physics and Department of Physics and Astronomy,  
University of California Los Angeles, Los Angeles, California 90095, USA

 (Received 17 May 2019; revised manuscript received 7 August 2019; published 27 August 2019)

We investigate the effect that density wave states have on the Hofstadter butterfly. We first review the problem of the  $d$ -density wave on a square lattice and then numerically solve the  $d$ -density wave problem when an external magnetic field is introduced. As the  $d$ -density wave condensation strength is tuned the spectrum evolves through three topologically distinct butterflies, and a relativistic quantum Hall effect is observed. The chiral  $p + ip$ -density wave state demonstrates drastically different Hofstadter physics—inducing a destruction of the gaps in the butterfly which causes electrons' cyclotron orbits to not obey any type of Landau quantization, and the creation of a large gap in the spectrum with Hall conductance  $\sigma_{xy} = 0$ . To investigate the quantum phases in the system we perform a multifractal analysis of the single particle wave functions. We find that tuning the  $d$ -density wave strength at a generic value of magnetic flux controls a metal-metal transition at charge neutrality where the wave-function multifractality occurs at energy level crossings. In the  $p + ip$  case we observe another metal-metal transition occurring at an energy level crossing separated by a strongly multifractal quasi-insulating island state occurring at charge neutrality and strip dimerization of the lattice.

DOI: [10.1103/PhysRevB.100.075150](https://doi.org/10.1103/PhysRevB.100.075150)

### I. INTRODUCTION

When electrons in two dimensions are subjected to both a periodic potential of a crystalline lattice and a uniform magnetic field the two competing length scales, that of the Landau cyclotron orbits and that of the crystalline lattice, give rise to quantum fractal spectra. This system has provided an interesting basis for much research over the years. The effects of mutual Coulomb interactions in GaAs [1] and graphene [2,3] have been considered, as well as disorder [4], impurity effects [5], and much more. Despite the beauty and the complexity of the structure it has remained somewhat elusive because these length scales are typically severely mismatched. Advances in experimentally measuring the fractal energy spectrum in GaAs heterostructures [6,7] as well as in the moiré superlattice of bilayer graphene [8] have opened up the possibility of investigating emergent behavior within a fractal landscape. Furthermore, the theoretical study of the unconventional superconductivity recently detected in slightly twisted bilayer graphene [9] has predicted electronic ordering instabilities which favor density wave states [10]. Motivated by these results we investigate the effect density waves have on the Hofstadter butterfly.

Unlike Cooper pair condensation (particle-particle condensation) density wave states are comprised of particle-hole condensates. The particle-hole condensate wave function does not have to obey the same spin/orbital antisymmetry requirements that Cooper pair wave functions do because particles and holes are distinct objects. A particularly interesting density wave state is the  $d_{x^2-y^2}$ -density wave, also known as the staggered flux state. The staggered flux state breaks time-reversal symmetry and is visualized as a series of staggered currents on the bonds of the square lattice [11] (see Fig. 1). We briefly review particle-hole condensation in this angular momentum channel on the square lattice in the following.

On the mean-field level the single-particle Hamiltonian for electrons in an external magnetic field with singlet particle-hole pairing in the  $d_{x^2-y^2}$  channel on the square lattice in position space is written as [12,13]

$$\begin{aligned}
 H = \sum_{n,m} & \left( -t_1 + i \frac{W_0}{4} (-1)^{n+m} \right) e^{i\phi_x} |m+1, n\rangle \langle m, n| \\
 & + \left( -t_2 - i \frac{W_0}{4} (-1)^{n+m} \right) e^{i\phi_y} |m, n+1\rangle \langle m, n| \\
 & - t_3 e^{i\phi_{xy}} |m+1, n+1\rangle \langle m, n| \\
 & - t_4 e^{i\phi_{yx}} |m+1, n-1\rangle \langle m, n| + \text{H.c.}, \quad (1)
 \end{aligned}$$

where each  $\phi$  is the Peierls phase associated with each unique hopping element,  $W_0$  is the  $d$ -density wave strength, we subtracted off the chemical potential, and we included only nearest neighbor (NN) and next-nearest neighbor (NNN) terms. For the remainder of the paper we take  $t_1 = t_2 = t$ , and omit spin indices.

When there is no external magnetic field present the staggered flux causes the unit cell's size to double—comprised of an  $n + m = \text{even}$ ,  $n + m = \text{odd}$ . Ignoring NNN hopping we write the Hamiltonian in the absence of external magnetic field as

$$\begin{aligned}
 H = -\tilde{t} \sum_{n,m} & e^{-2i\alpha_{nm}} |m+1, n\rangle \langle m, n| \\
 & + |m, n+1\rangle \langle m, n| + \text{H.c.}, \quad (2)
 \end{aligned}$$

where we have a new variable,  $\tilde{t} = \sqrt{t^2 + (W_0/4)^2}$ , and  $\alpha_{nm} = \arctan(W_0/4t)(-1)^{n+m}$ . In this language the dispersion is written as

$$E = \pm 2\tilde{t} \sqrt{\cos^2(k_x) + \cos^2(k_y) + 2\cos(2\alpha)\cos(k_x)\cos(k_y)}, \quad (3)$$

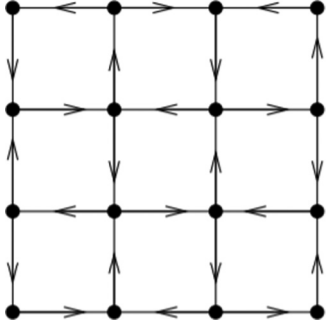


FIG. 1. Real space lattice corresponding to the  $d_{x^2-y^2}$  state. Arrowed lines indicate current.

where  $\alpha = |\alpha_{nm}|$  and

$$\cos(2\alpha) = \frac{1 - (W_0/4t)^2}{1 + (W_0/4t)^2}. \quad (4)$$

We see that as the density wave strength is tuned on from 0 the dispersion evolves smoothly from the free electron case to the  $\pi$ -flux fermion case at  $\alpha = \pi/4$ . With this in mind we rewrite the Hamiltonian in the suggestive form

$$H = -\tilde{t} \sum_{n,m} e^{-2i\alpha_{nm}} |m+1, n\rangle \langle m, n| + (\cos^2(2\alpha) + \sin^2(2\alpha)) |m, n+1\rangle \langle m, n| + \text{H.c.}, \quad (5)$$

which is equivalent to

$$H = \cos(2\alpha)H_0 + \sin(2\alpha)H_\pi, \quad (6)$$

where

$$H_0 = -\tilde{t} \sum_{n,m} |m+1, n\rangle \langle m, n| + \cos(2\alpha) |m, n+1\rangle \langle m, n| + \text{H.c.}, \quad (7)$$

and

$$H_\pi = -\tilde{t} \sum_{n,m} -i(-1)^{m+n} |m+1, n\rangle \langle m, n| + \sin(2\alpha) |m, n+1\rangle \langle m, n| + \text{H.c.} \quad (8)$$

Here,  $H_0$  is a typical tight binding Hamiltonian, and  $H_\pi$  is a Hamiltonian for  $\pi$ -flux fermions.

## II. BUTTERFLIES

### A. Nearest neighbors

Turning on an external magnetic field in the  $d$ -density wave problem amounts to the usual Peierls substitution [14]. Taking the Landau gauge  $\vec{A} = (-By, 0, 0)$ , the  $m$  direction hopping elements in the Hamiltonian [Eq. (6)] are modified via  $|m+1, n\rangle \rightarrow e^{-i2\pi n\Phi/\Phi_0} |m+1, n\rangle$ , where  $2\pi\Phi/\Phi_0$  is the dimensionless magnetic flux penetrating an elementary plaquette. We numerically diagonalize the Hamiltonian on a  $20 \times 20$  lattice using periodic boundary conditions and plot the energy (in units of  $t$ ) versus  $\Phi/\Phi_0$  at the highest symmetry in Figs. 2, 3, and 4.

When  $\alpha = 0$  we recover the usual Hofstadter butterfly, and when  $\alpha = \pi/4$  we recover the  $\pi$ -shifted butterfly governed by

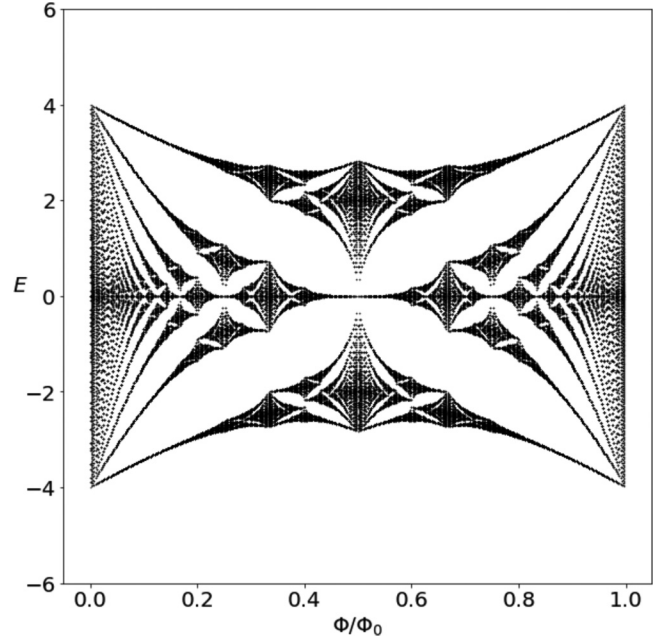


FIG. 2. Plot of the butterfly for  $\alpha = 0$ .

the form of Eq. (8). As  $\alpha$  is tuned away from 0, linear Landau levels emerge from the edges of the spectrum at  $\pi$  flux, and relativistic levels emerge at 0 and  $2\pi$  flux at charge neutrality yielding a spectrum similar to that of the honeycomb lattice [15]. All emerging Landau levels are accompanied by gap openings with odd Chern number, which will be discussed further in the following section. The relativistic Landau level energy eigenvalues emerging from 0 flux are given by (see the Appendix)

$$\epsilon_n = \pm 2\sqrt{\frac{e_0 B |W_0| t}{c}} n. \quad (9)$$

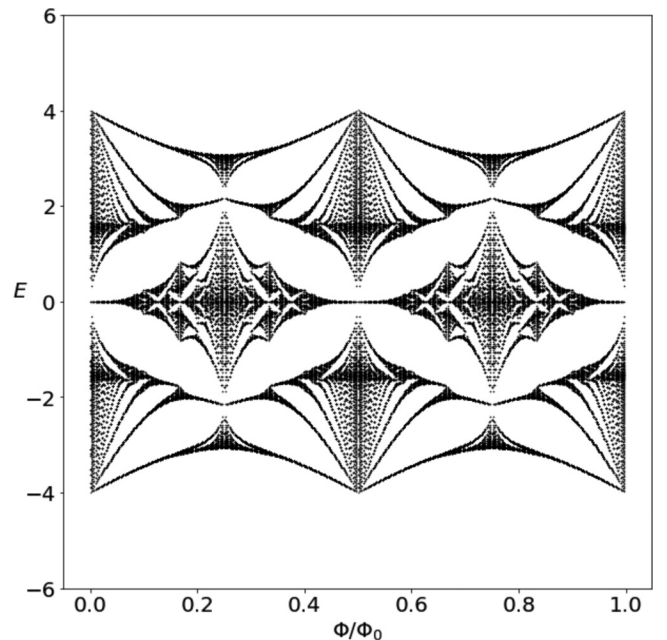
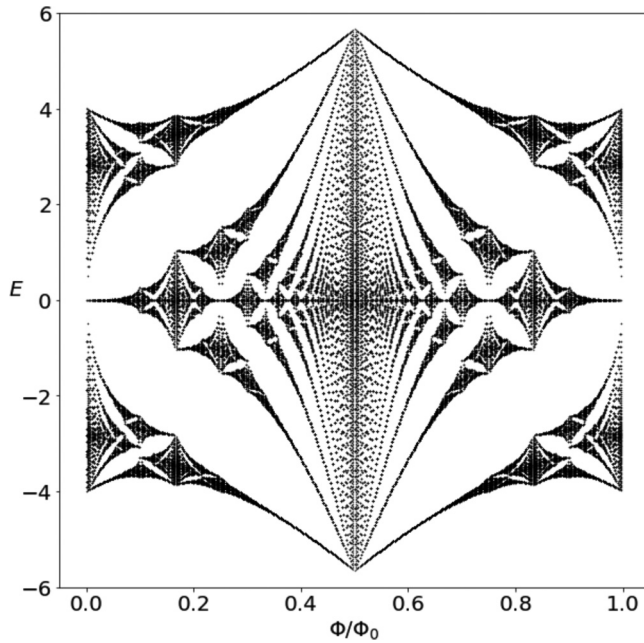


FIG. 3. Plot of the butterfly for  $\alpha = \pi/8$ .


 FIG. 4. Plot of the butterfly for  $\alpha = \pi/4$ .

As  $W_0$  is tuned from 0 to  $4t$  the Hall conductances,  $\sigma_{xy}$ , change for a given flux and Fermi energy. Due to the global nature of the transformation of the topological phase diagram (the Hofstadter butterfly) we categorize the topologically different types of butterflies instead of investigating topological phase transitions local to a given flux and Fermi energy in the following section.

### B. Topological maps of the $d_{x^2-y^2}$ -density wave butterfly

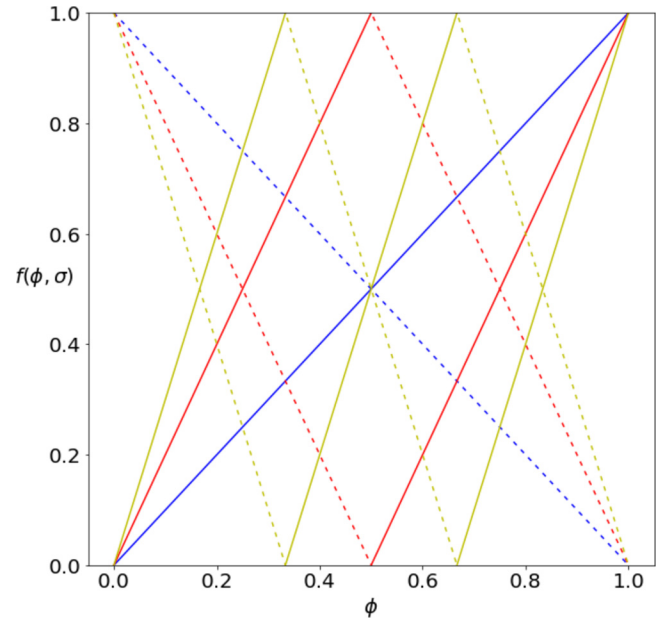
To characterize the defining topological characteristics of each butterfly we start with the extremum of the transformation controlled by the density wave strength. First of all, consider the situation when  $\alpha = \pi/4$ . Directly from our Gauge-transformed Hamiltonian we see that the total flux penetrating a plaquette is  $\Phi \pm 4|\alpha| = \Phi \pm \pi$ , where the plus or minus indicates that we are at an even/odd plaquette, respectively. Thus the Hamiltonian can be written as

$$H = -\sqrt{2}t \sum_{n,m} e^{-i(\Phi+\pi)n} |m+1, n\rangle \langle m, n| + |m, n+1\rangle \langle m, n| + \text{H.c.}, \quad (10)$$

because the Hamiltonian in the absence of density wave condensation is symmetric about  $\Phi = \pm\pi$ .

This observation explicitly shows that the density wave parameter  $W_0$  controls a smooth transformation between the typical butterfly and the  $\pi$ -shifted, or butterfly. The Hall conductances for the gaps can be written down immediately for these two extremum of the transformation via a Diophantine equation [16], but because the particular Diophantine equation which governs the region  $0 < \alpha < \pi/4$  is not immediately obvious we follow a different prescription.

To describe the global distribution of Chern numbers in the gaps of the butterflies we closely follow work done by Naumis [17] on the ‘‘Cut and Projection’’ solution to the Diophantine


 FIG. 5. Skeleton of the butterfly for  $\alpha = 0$ . Solid (dashed) blue lines correspond to  $\sigma_{xy} = 1$  ( $-1$ ), solid (dashed) red lines correspond to  $\sigma_{xy} = 2$  ( $-2$ ), and solid (dashed) yellow lines correspond to  $\sigma_{xy} = 3$  ( $-3$ ).

equation

$$\sigma_r = q \left\{ \phi r + \frac{1}{2} \right\} - \frac{q}{2}. \quad (11)$$

Here  $\sigma$  is the Hall conductance,  $r$  is the gap index, the curly braces indicate taking the fractional part of the quantity contained, and  $\phi = \Phi/\Phi_0 = p/q$  where  $p/q$  is a fully reduced fraction. The filling factor for a gap’s Chern number at a given flux is defined as

$$f(\phi, \sigma) = \{\phi\sigma_r\}. \quad (12)$$

Plotting  $f(\phi, \sigma)$  against the flux yields the Wannier diagram [18], or the ‘‘skeleton,’’ of the butterfly. The form of  $f(\phi, \sigma)$  dictates the distribution of Hall conductances in the gaps of the butterflies. We find the skeletons for  $\alpha = 0, \pi/4$  using this solution to the Diophantine equation (see Figs. 5 and 6).

To construct the Wannier diagram for values of  $0 < \alpha < \pi/4$  we note the following: As soon as  $W_0$  is nonzero all gaps that are not associated with the normal butterfly, but are associated with the  $\pi$ -flux butterfly, emerge (in the Appendix we see that regardless of how small  $W_0$  is all Landau levels indexed by  $n$  emerge). Furthermore, the Chern numbers associated with all gaps are topological invariants and thus will not change due to perturbations to the Hamiltonian. Taking these facts into account we draw the topological map for the region  $0 < \alpha < \pi/4$  as the combination of the two extremum butterfly skeletons—see Fig. 7. Because our topological map is a combination of the normal butterfly skeleton and the  $\pi$ -shifted butterfly skeleton we see a doubling of lines associated with odd Hall conductances, while the even Hall conductances remain stationary.

At  $\alpha = 0, \pi/4, \pi/2$  the odd numbered Hall band doubling disappears and one is left with topological maps associated

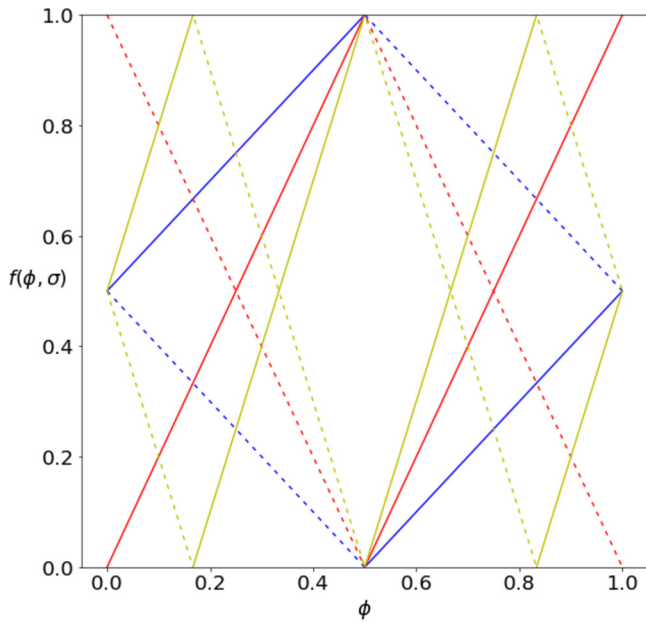


FIG. 6. Skeleton of the butterfly for  $\alpha = \pi/4$ . Solid (dashed) blue lines correspond to  $\sigma_{xy} = 1$  ( $-1$ ), solid (dashed) red lines correspond to  $\sigma_{xy} = 2$  ( $-2$ ), and solid (dashed) yellow lines correspond to  $\sigma_{xy} = 3$  ( $-3$ ).

with Fig. 5. Notice, however, that  $\alpha = \pi/2$  is an unphysical region in which  $W_0/t \rightarrow \infty$ . Thus we see that there are three topologically distinct phase diagrams associated with the

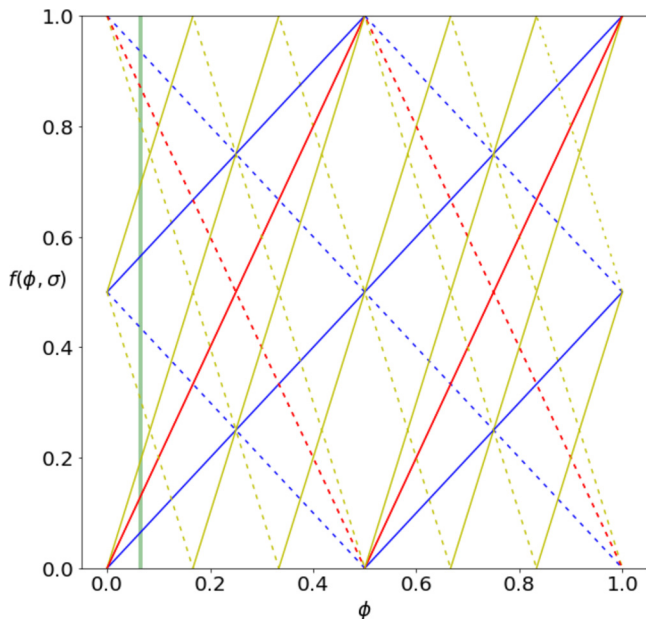


FIG. 7. Skeletons of the butterflies for  $0 < \alpha < \pi/4$ . Solid (dashed) blue lines correspond to  $\sigma_{xy} = 1$  ( $-1$ ), solid (dashed) red lines correspond to  $\sigma_{xy} = 2$  ( $-2$ ), and solid (dashed) yellow lines correspond to  $\sigma_{xy} = 3$  ( $-3$ ). The vertical green line acts as a guide, indicating that for the regime  $0 < W_0 < 4t$ , at a fixed flux, one would cross double the amount of odd Chern numbered gaps than those of the typical butterfly as one tunes the Fermi energy from the minimum value of the dispersion's energy to its maximum.

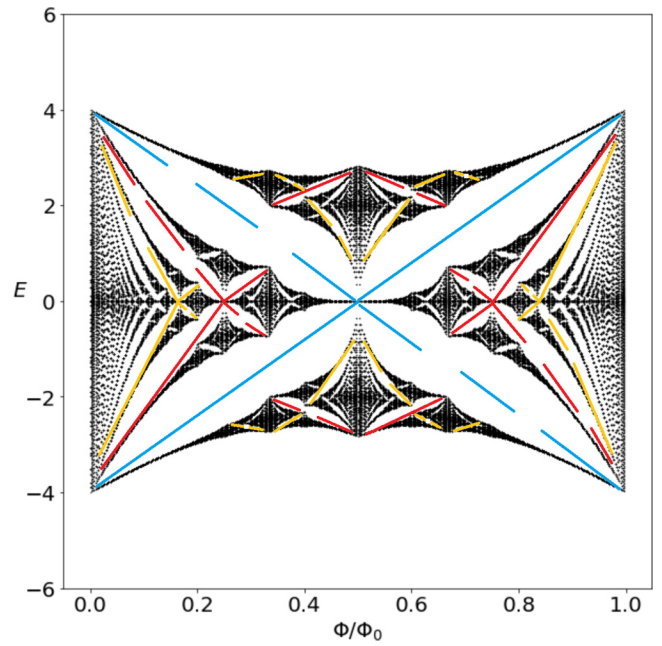


FIG. 8. Butterfly with labeled characteristic Hall conductances for  $\alpha = 0$ . Solid (broken) blue lines correspond to  $\sigma_{xy} = 1$  ( $-1$ ), solid (broken) red lines correspond to  $\sigma_{xy} = 2$  ( $-2$ ), and solid (broken) yellow lines correspond to  $\sigma_{xy} = 3$  ( $-3$ ).

$d$ -density wave problem in an external magnetic field, and that these maps change only at  $W_0 = 0$ , and  $W_0 = 4t$ .

Using the structure of our obtained diagrams as a guide we label the Hall conductances for all gaps associated with all butterflies (see Figs. 8, 9, and 10). Due to the odd Hall conductance line doubling for  $0 < \alpha < \pi/4$  there exists a

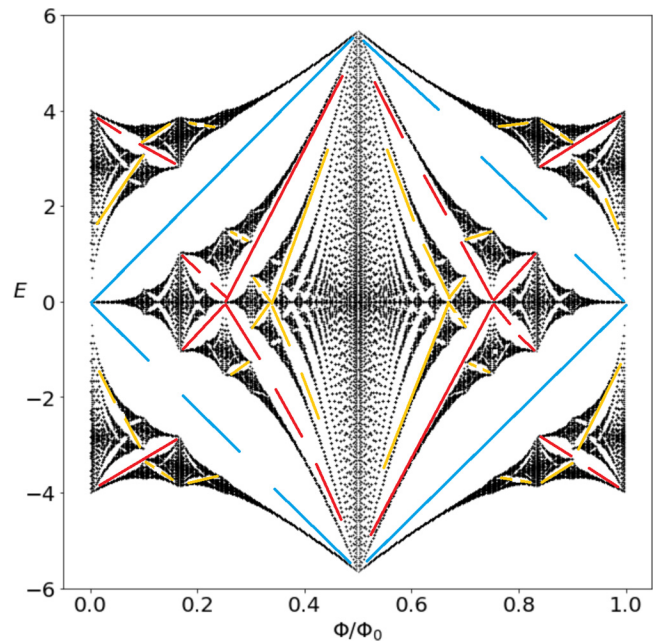


FIG. 9. Butterfly with labeled characteristic Hall conductances for  $\alpha = \pi/4$ . Solid (broken) blue lines correspond to  $\sigma_{xy} = 1$  ( $-1$ ), solid (broken) red lines correspond to  $\sigma_{xy} = 2$  ( $-2$ ), and solid (broken) yellow lines correspond to  $\sigma_{xy} = 3$  ( $-3$ ).

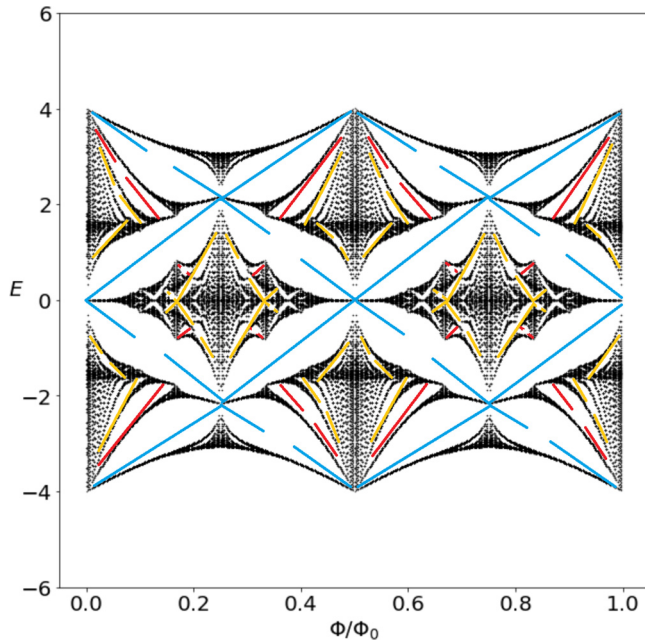


FIG. 10. Butterfly with labeled characteristic Hall conductances for  $\alpha = \pi/8$ . Solid (broken) blue lines correspond to  $\sigma_{xy} = 1$  ( $-1$ ), solid (broken) red lines correspond to  $\sigma_{xy} = 2$  ( $-2$ ), and solid (broken) yellow lines correspond to  $\sigma_{xy} = 3$  ( $-3$ ).

relativistic quantum Hall effect at low fields near charge neutrality (akin to that of graphene [19]) in the sense that the Hall conductances are quantized via

$$\sigma_{xy} = \pm \frac{e^2}{h} 2(2N + 1), \quad (13)$$

where  $N$  is an integer and we included a factor of 2 due to spin degeneracy. The typical integer quantum Hall conductances persist at the edges of the spectrum near 0 flux and the odd Chern numbered gaps only disappear completely when  $\alpha = \pi/4$  where the remaining gaps have

$$\sigma_{xy} = \pm \frac{e^2}{h} 2(2N), \quad (14)$$

where, again, we multiplied by a factor of 2 due to spin degeneracy.

### III. $p + ip$ DENSITY WAVE ORDER

The singlet  $\vec{Q} = (0, \pi)$   $p_x + ip_y$ -density wave state also breaks translation and time-reversal symmetry, and is visualized as both a series of staggered currents pointing along the  $x$  direction, and bonds of zero net current that connect nearest neighbors along the  $y$  direction [11] (see Fig. 11). For this  $\vec{Q} = (0, \pi)$   $p_x + ip_y$ -density wave the Hamiltonian is

$$H = \sum_{n,m} \left( -t - i \frac{W_0}{2} (-1)^n \right) e^{i\phi_x} |m+1, n\rangle \langle m, n| + \left( -t + \frac{W'_0}{2} (-1)^n \right) e^{i\phi_y} |m, n+1\rangle \langle m, n| + \text{H.c.}, \quad (15)$$

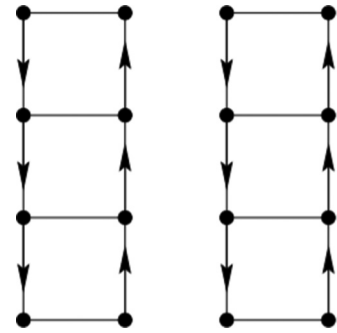


FIG. 11. Real space lattice corresponding to the  $p_x + ip_y$  density wave state. Arrowed lines indicate current whereas arrowless lines indicate bonds with no net current with energetically favored hopping.

where the density wave order parameter is

$$\langle \psi^\dagger(\vec{k} + \vec{Q}) \psi(\vec{k}) \rangle = \pm (W_0 \sin(k_x) + iW'_0 \sin(k_y)). \quad (16)$$

In the following we take  $W_0 = W'_0$ , and define  $\alpha = \arctan(\frac{W_0}{2t})$ . We plot the butterflies at two characteristic points for a  $20 \times 20$  lattice in Figs. 12 and 13. We see that chiral  $p$ -density wave condensation breaks the butterfly's reflection symmetry about  $\pi$  flux, opens bubbles of  $\sigma_{xy} = 0$ , and causes major band gaps to collapse (a phenomenon well known to occur in lattices with anisotropic hoppings [20])—in fact, at  $\alpha = \pi/4$ , when the system is completely dimerized along the  $y$  direction and the lattice is composed of disjointed  $2 \times L$  ( $L$  being the side length of the lattice along the  $x$  direction in units of the lattice constant) cylindrical strips of alternating density-wave-induced fluxes, we find that the butterfly is completely destroyed and all gaps have collapsed except for a major gap near charge neutrality emanating from  $\pi$  flux. For the  $p - ip$ -density wave case the spectrum is obtained via a reflection of

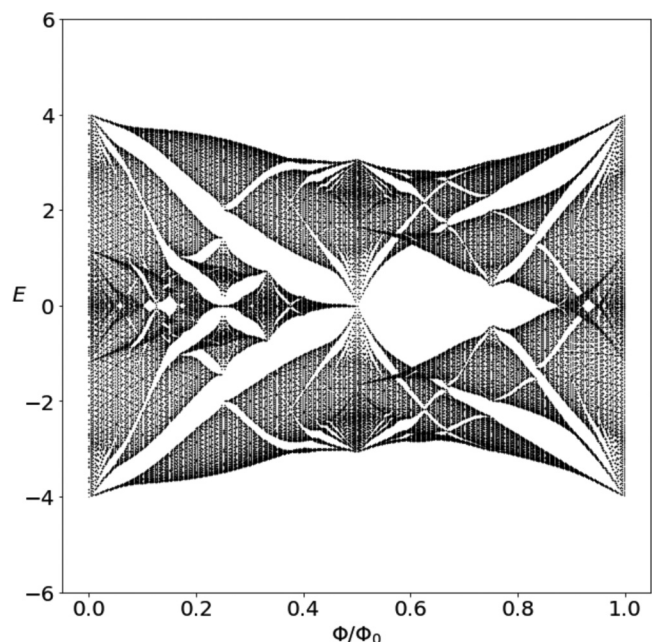
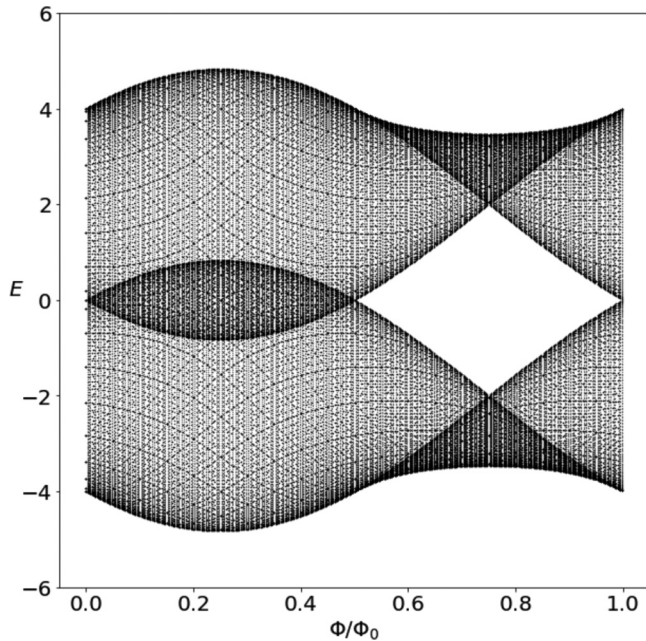


FIG. 12. Plot of the butterfly for  $\alpha = \pi/8$ .

FIG. 13. Plot of the butterfly for  $\alpha = \pi/4$ .

the  $p + ip$  spectrum about  $\pi$  flux—implying that the  $\sigma_{xy} = 0$  gap would be detectable at modest magnetic field strengths. For either type of chiral  $p$ -wave condensation at  $W_0 = 2t$  the electrons would not obey any type of Landau quantization of their cyclotron orbits. Furthermore, because Chern numbers follow a “zero sum” rule, this major gap at  $\alpha = \pi/4$  must have  $\sigma_{xy} = 0$ —thus, using the arguments highlighted in the previous section, the topological map of Hall conductances associated with this density wave state for  $0 < W_0 < 2t$  is given by the typical square lattice skeleton (Fig. 5) and a  $f(\phi, \sigma) = 0$  line.

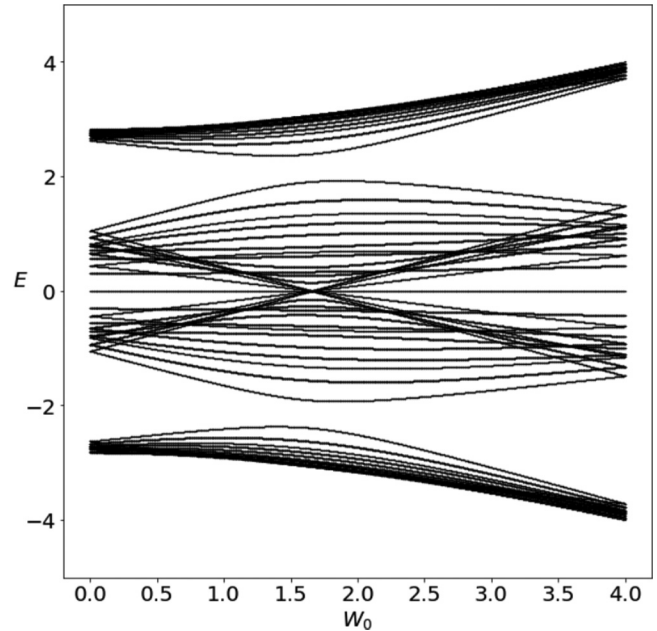
#### IV. MULTIFRACTAL ANALYSIS

Multifractality is a defining characteristic of wave function fluctuations at criticality [21]. In the following we investigate the nature of the quantum phase transitions that occur as we increase the density wave strength utilizing a basic multifractal analysis of the generalized inverse participation ratio. Via this procedure we find that, at a fixed value of magnetic flux, the zero-energy eigenfunctions undergo metal-metal transitions separated by energy level crossings and single-particle wave function multifractality.

The generalized inverse participation ratio (IPR) scales with the system size

$$P_q = \sum_{m,n} |\psi(r_{m,n})|^{2q} \sim L^{-\tau(q)} \quad (17)$$

at a fixed energy, where the summation is taken over the real space lattice defined by  $r_{m,n}$ . The exponents  $\tau(q)$ , indexed by a continuous variable  $q$ , are given by  $\tau(q) = D_q(q - 1)$ , where  $D_q = d$  for delocalized metallic states and  $D_q = 0$  for exponentially localized insulating states. Exponents  $\tau(q)$  that depend on  $q$  in a nonlinear fashion indicate wave function multifractality. In our analyses we focus on the behavior of the system near charge neutrality—thus, to obtain the wave

FIG. 14. Energy versus  $d$ -density wave strength calculated at  $\Phi/\Phi_0 = 1/4$  for a  $28 \times 28$  lattice.

functions pertinent to Eq. (17), we diagonalize the magnetic Hamiltonian in real space (as we did when plotting the butterflies) and find the corresponding zero energy eigenvectors of the system for a fixed pair of  $\Phi$  and  $W_0$ .

We choose values of  $\Phi/\Phi_0$  such that there exists a zero energy eigenvalue for all  $W_0$ . Numerically there is a difficulty in calculating the IPR of a single degenerate energy eigenvector. To remedy this we add a small amount of flux  $\Delta = 1 \times 10^{-15}$  to  $\Phi/\Phi_0$  which does not alter the spectrum, or eigenvectors in any appreciable manner but does separate (on the order of  $\Delta$ ) the degenerate zero energy eigenvalues from one another enough for us to calculate the IPR of a single zero energy eigenvector as a function of  $W_0$  without mixing in the IPR of the other degenerate zero energy eigenvectors.

As  $W_0$  is tuned a level crossing occurs in the spectrum. At this (highly degenerate) crossing point the Chern numbers of the bands participating are no longer well defined, but still follow the requirement that the sum of all Cherns in the spectrum is zero. For a  $28 \times 28$  lattice we plot both the spectrum and the  $\text{IPR}(q = 2)$  at  $\Phi/\Phi_0 = 1/4 + \Delta$  (see Figs. 14 and 15). All listed values of  $W_0$  are in units of  $t$ . At this particular flux there is an energy level crossing which occurs at  $W_0^* = 4 \tan(\frac{\pi}{8})$  which is accompanied by a singular behavior of the  $\text{IPR}(q = 2)$ —indicating a rapid change in the behavior of the single-particle wave function fluctuations at the point where the energy levels touch. We find that the multifractal exponents reveal that the zero energy wave functions demonstrate multifractality at  $W_0^*$ —see Fig. 16. The behavior of the multifractal exponents at this critical point indicate a weakly multifractal behavior (sometimes dubbed “quasimetallic”) with  $\tau(q)$ ’s leading nonlinear dependence (found using a least squares fitting method)  $\approx -0.115q(q - 1)$  in the region  $0 < q < 3$ . Furthermore, we find that on either side of the critical point  $\tau(q) \approx 2(q - 1)$  which is a signature of delocalized metallic states in two spatial dimensions. Due

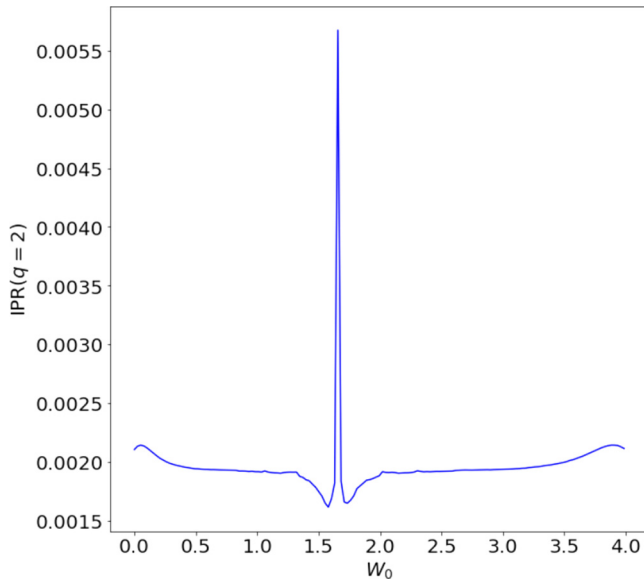


FIG. 15. Numerically calculated IPR ( $q = 2$ ) as a function of  $W_0$  of one of the zero energy wave functions for a  $28 \times 28$  lattice at  $\Phi/\Phi_0 = 1/4 + \Delta$ .

to both the level crossing and the real space multifractality of the wave functions near the central peak shown in Fig. 15, we find that the  $d$ -density wave strength controls a metal-metal transition at  $\Phi/\Phi_0 = 1/4 + \Delta$  at charge neutrality.

Physically this critical point, which is generally given by  $W_0^* = 4t \tan(\pi \frac{\Phi}{2\Phi_0})$  for arbitrary  $\Phi/\Phi_0$ , marks the point at which the local effective magnetic fields penetrating neighboring plaquettes flip from aligned to anti-aligned (see Fig. 17). This can be seen directly by calculating the total effective dimensionless flux  $2\pi \Phi_T/\Phi_0$  per plaquette utilizing the phase

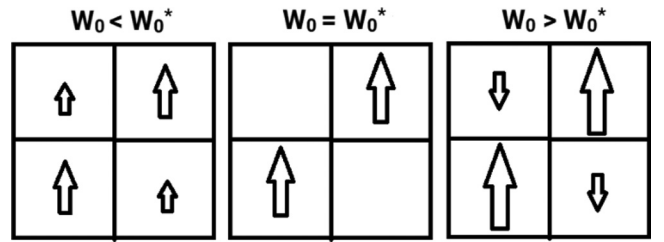


FIG. 17. Pictorial representation of the local magnetic field (perpendicular to the lattice) per plaquette for different values of  $W_0$  for the  $d$ -density wave case. The size of the arrow indicates the strength of the field.

factor in Eq. (2)

$$2\pi \Phi_T/\Phi_0 = 2\pi \Phi/\Phi_0 \pm 4\alpha. \quad (18)$$

For  $W_0 < W_0^*$  the flux per plaquette is alternating but always positive. At  $W_0 = W_0^*$  the flux alternates between  $4\pi \Phi/\Phi_0$  and 0. For  $W_0 > W_0^*$  the total effective flux per plaquette is alternating in magnitude and sign (see Fig. 17).

For the case of  $p + ip$ -density wave condensation wave functions tend to behave in a localized fashion at  $W_0 = 2$  for all  $\Phi > 0$  due to the dimerization that occurs in the lattice along the  $y$  direction. We calculate the wave functions' multifractal exponents near charge neutrality as we did in the  $d$ -density wave case and plot the spectrum and IPR with  $\Phi$  fixed in Figs. 18 and 19. The wave functions in this case display strong multifractality at  $W_0 = 2$  (see Fig. 20) where the electrons are strongly localized to a strip of the lattice and there is another level crossing similar to that observed in the  $d$ -density wave case. For  $W_0 = 2$  we find the nonlinear dependence of  $\tau(q) \approx 0.503q^2 + 2.60\sqrt{q}$  for  $0 < q < 1$  using the fitting method mentioned above.

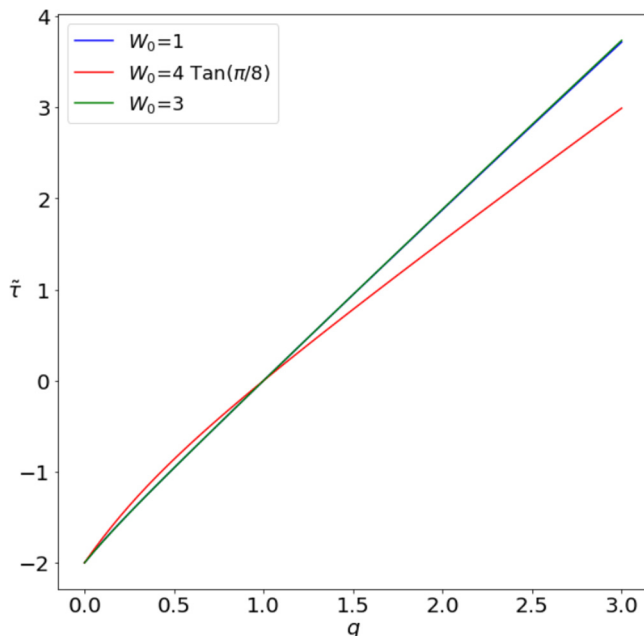


FIG. 16. Values of  $-\ln(P_q)/\ln(L) = \tilde{\tau}(q)$  calculated for a  $28 \times 28$  lattice at  $\Phi/\Phi_0 = 1/4 + \Delta$  for three characteristic values of  $W_0$ .

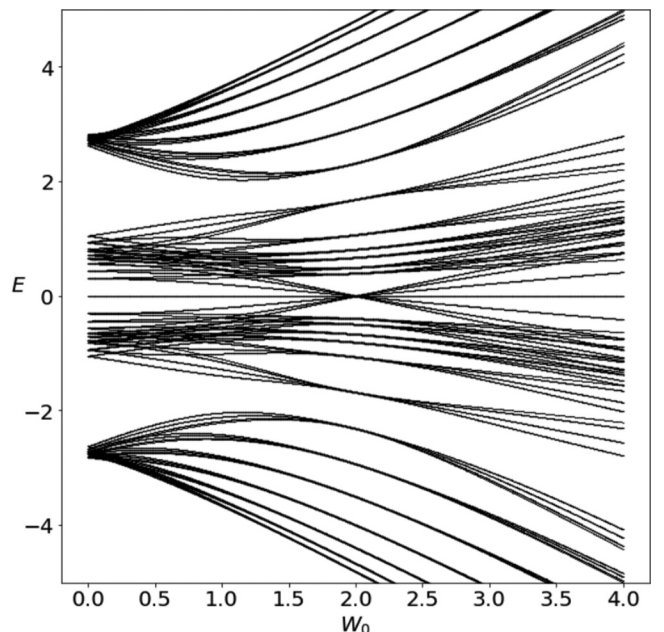


FIG. 18. Energy versus  $p + ip$ -density wave strength calculated at  $\Phi/\Phi_0 = 1/4$  for a  $28 \times 28$  lattice.

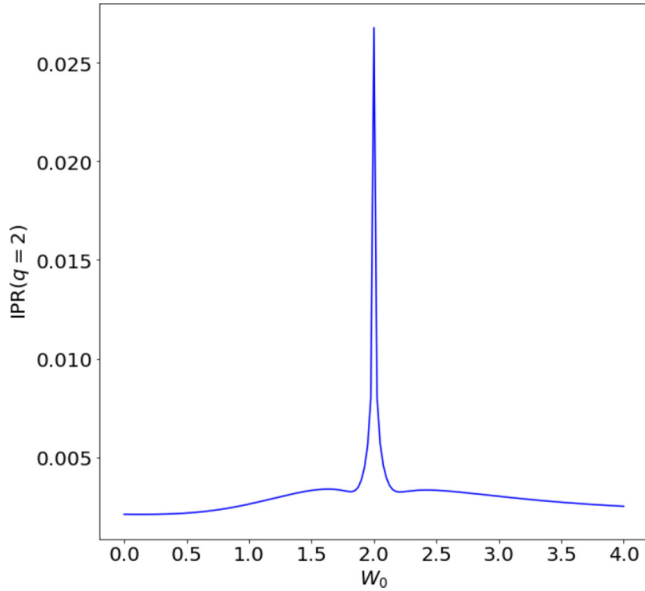


FIG. 19. Numerically calculated IPR ( $q = 2$ ) as a function of  $W_0$  of one of the zero energy wave functions for a  $28 \times 28$  lattice at  $\Phi/\Phi_0 = 1/4 + \Delta$ .

## V. DISCUSSION

In this work we studied and characterized the topologically different forms of the Hofstadter butterflies generated in the presence of density wave condensations in the  $d_{x^2-y^2}$ , and  $p_x \pm ip_y$  angular momentum channels and investigated the quantum phase transitions that occur at charge neutrality as density wave strength increases. Directly from the skeleton diagrams obtained for the  $d_{x^2-y^2}$ -density wave problem we see a doubling in the odd-Hall conductance lines which implies that the density wave strength controls a relativistic quantum

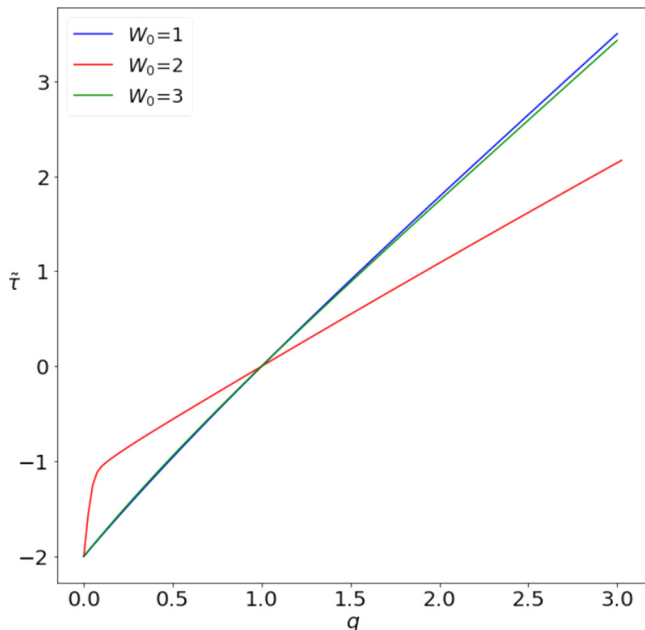


FIG. 20. Values of  $-\ln(P_q)/\ln(L) = \tilde{\tau}(q)$  calculated for a  $28 \times 28$  lattice at  $\Phi/\Phi_0 = 1/4 + \Delta$  for three characteristic values of  $W_0$ .

Hall effect with  $\sigma_{xy} = \pm \frac{e^2}{h} 2(2N + 1)$ . Furthermore, we find that the  $p + ip$ -density wave both causes band gap collapses in the butterfly, and causes the opening of 0 Hall conductivity bubbles. The effects of density wave states in the presence of an external magnetic field can be detected both at modest magnetic field strengths in two-dimensional square crystal lattices (via a measurement of an unusual quantum Hall effect for the  $d$ -wave, or via a measurement of the system which shows both a lack of Landau levels and the opening of  $\sigma_{xy} = 0$  gaps near charge neutrality), and in optical lattice systems with the appropriate staggered fluxes present.

Our results show that different types of metal-metal transitions, controlled by density wave strength and separated in phase space by single-particle wave functions exhibiting multifractality, would be detectable in systems emulating density wave states at nonzero flux at half filling. These quantum phase transitions occur generically for both density wave condensations due to the nonanalyticity introduced when the energy levels cross in the spectrum at strip dimerization for  $p + ip$ -density waves, or at the critical value of the staggered flux at  $W_0^* = 4 \tan(\frac{\pi\Phi}{2\Phi_0})$  for  $d$ -density waves. We note that in the presence of moderate disorder the energy levels would be broadened but the physics outlined in our work would be effectively the same—the effects of strong disorder, on the other hand, should be considered in future work. Furthermore, future work might also investigate how mutual Coulomb interactions would affect the multifractal wave functions and quantum phase transitions that occur as a function of density wave strength.

## ACKNOWLEDGMENTS

We would like to thank Steven Durr for helpful discussions.

## APPENDIX: LANDAU LEVELS

To see how the relativistic Landau levels emerge in the spectrum we follow the standard analysis [22] and expand the tight binding Hamiltonian in the even-odd basis

$$H_0(\vec{k}) = -2\tilde{t} \begin{bmatrix} 0 & e^{-2i\alpha} \cos(k_x) + \cos(k_y) \\ e^{2i\alpha} \cos(k_x) + \cos(k_y) & 0 \end{bmatrix}, \quad (\text{A1})$$

about one of the charge neutrality points  $\vec{k} = (\pi/2, \pi/2)$

$$H_0(\vec{k}) \approx 2\tilde{t} \begin{bmatrix} 0 & e^{-2i\alpha} k_x + k_y \\ e^{2i\alpha} k_x + k_y & 0 \end{bmatrix}. \quad (\text{A2})$$

When introducing a magnetic field one makes the substitution

$$k_x \rightarrow k_x + \frac{eBy}{c} = \tilde{k}_x, \quad (\text{A3})$$

where  $e$  is the electron's charge and  $c$  is the speed of light. Because  $\hat{k}_y$  and  $\hat{y}$  do not commute with one another we place hats on all crystal momentum and position variables in the Hamiltonian with the understanding that we will work in the real space ( $\hat{k}_y = -i\partial_y$ ) representation of these operators



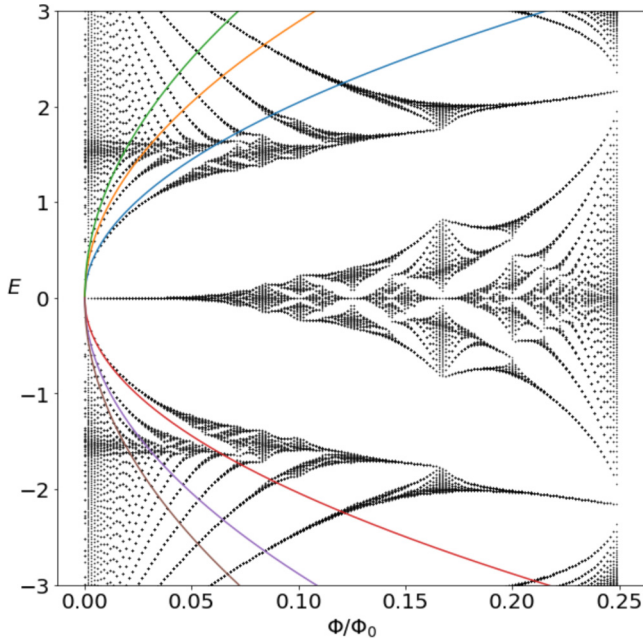


FIG. 21. Plot of the butterfly and the associated first few nonzero Landau levels for  $\alpha = \pi/8$ .

henceforth. Rearranging the Schrödinger equation

$$2\tilde{t} \begin{bmatrix} 0 & e^{-2i\alpha}\hat{k}_x + \hat{k}_y \\ e^{2i\alpha}\hat{k}_x + \hat{k}_y & 0 \end{bmatrix} \begin{bmatrix} \psi_n \\ \phi_n \end{bmatrix} = \epsilon_n \begin{bmatrix} \psi_n \\ \phi_n \end{bmatrix} \quad (\text{A4})$$

yields two decoupled wave equations

$$\epsilon_n^2 \psi_n = 4\tilde{t}^2 (e^{-2i\alpha}\hat{k}_x + \hat{k}_y)(e^{2i\alpha}\hat{k}_x + \hat{k}_y)\psi_n, \quad (\text{A5})$$

$$\epsilon_n^2 \phi_n = 4\tilde{t}^2 (e^{2i\alpha}\hat{k}_x + \hat{k}_y)(e^{-2i\alpha}\hat{k}_x + \hat{k}_y)\phi_n. \quad (\text{A6})$$

For the time being we solve Eq. (A5). Foiling out this wave equation we yield

$$\begin{aligned} \frac{\epsilon_n^2}{4\tilde{t}^2} \psi_n(y, k_x) = & \left( \left( \hat{k}_x + \frac{eB\hat{y}}{c} \right)^2 + \hat{k}_y^2 \right. \\ & + \cos(2\alpha) \left\{ \hat{k}_x + \frac{eB\hat{y}}{c}, \hat{k}_y \right\} \\ & \left. - i \sin(2\alpha) \frac{eB}{c} [\hat{y}, k_y] \right) \psi_n(y, k_x), \quad (\text{A7}) \end{aligned}$$

where we used the fact that  $[\hat{k}_x, \hat{k}_y] = 0$ .

We define

$$y_0 = k_x \frac{c}{e_0 B}, \quad \omega = \frac{e_0 B}{mc}, \quad (\text{A8})$$

where  $e_0$  is the absolute value of the electron charge  $e$ . Notice that because the Hamiltonian is independent of  $\hat{x}$  we can replace  $\hat{k}_x$  with its eigenvalue  $k_x$ . With these definitions in mind we rearrange Eq. (A7)

$$\begin{aligned} \frac{\epsilon_n^2}{8m\tilde{t}^2} \psi_n(y) = & \left( \frac{1}{2} m\omega^2 (y - y_0)^2 + \frac{1}{2m} \hat{k}_y^2 - \frac{\omega}{2} \sin(2\alpha) \right. \\ & \left. - \frac{\omega}{2} \cos(2\alpha) [y - y_0, \hat{k}_y] \right) \psi_n(y). \quad (\text{A9}) \end{aligned}$$

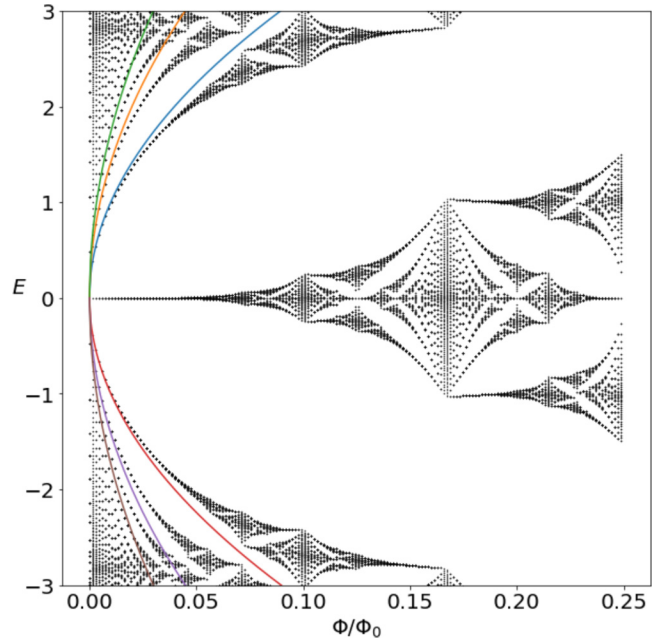


FIG. 22. Plot of the butterfly and the associated first few nonzero Landau levels for  $\alpha = \pi/4$ .

The solutions to this differential equation are of the form

$$\begin{aligned} \psi_n(y) = e^{im\omega(\frac{y^2}{2} - yy_0)e^{2i\alpha}} & \left\{ C_1 H_n[\sqrt{m\omega|\sin(2\alpha)}|(y - y_0)|] \right. \\ & \left. + C_2 {}_1F_1\left[-\frac{n}{2}; 1/2; (m\omega|\sin(2\alpha)|(y - y_0)^2)\right] \right\}, \quad (\text{A10}) \end{aligned}$$

where  $H_n(y)$  is the Hermite polynomial of degree  $n$  and  ${}_1F_1(-\frac{n}{2}; 1/2; y^2)$  is the Kummer confluent hypergeometric function. We find the energy eigenvalues of this system by requiring the index of the Hermite polynomials to be of integer value. Using this prescription we find

$$\epsilon_n = \pm \tilde{t} \sqrt{8|\sin(2\alpha)|m\omega n}, \quad (\text{A11})$$

or, in terms of the density wave condensation strength,

$$\epsilon_n = \pm 2\sqrt{\frac{e_0 B |W_0| t}{c}} n. \quad (\text{A12})$$

Solving Eq. (A6) in the same fashion yields shifted levels

$$\epsilon_n = \pm 2\sqrt{\frac{e_0 B |W_0| t}{c}} (n + 1), \quad (\text{A13})$$

where  $n = 0, 1, 2, 3, \dots$ , for both expressions. Due to the lack of the zero energy Landau level in Eq. (A13) we see that the single-particle wave functions will be nonzero only on the even sublattice for index  $n = 0$ , whereas wave functions will have nonzero amplitude on both even and odd sublattices for all  $n > 0$ .

Solving for the low energy behavior near the  $(k_x, k_y) = (-\pi/2, -\pi/2)$  Dirac point yields the same eigenenergy expressions obtained for the  $(\pi/2, \pi/2)$  case whereas we find the inverse of this even-odd behavior for the  $(k_x, k_y) = (\pi/2, -\pi/2)$ ,  $(-\pi/2, \pi/2)$  points. The Landau level expressions near these points can be obtained by flipping

the signs in front of both of the  $\cos(2\alpha)$ ,  $\sin(2\alpha)$  terms in Eq. (A9). In this case we find opposite wave function behavior—the single-particle wave functions will be nonzero only on the odd sublattice for index  $n = 0$ , and wave functions will have nonzero amplitude on both odd and even sublattices for all  $n > 0$ .

From this analysis we see that for  $W_0 \neq 0$  levels emerge from charge neutrality, regardless of the magnitude of  $W_0$ ; this is due to the  $d$ -density wave's symmetry breaking nature. We plot characteristic butterflies and the first few nonzero Landau levels according to Eqs. (A12) and (A13) in Figs. 21 and 22.

- 
- [1] V. Gudmundsson and R. R. Gerhardt, *Phys. Rev. B* **52**, 16744 (1995).
  - [2] V. M. Apalkov and T. Chakraborty, *Phys. Rev. Lett.* **112**, 176401 (2014).
  - [3] W. Luo and T. Chakraborty, *J. Phys.: Condens. Matter* **28**, 015801 (2016).
  - [4] J. G. Analytis, S. J. Blundell, and A. Ardavan, *Synth. Met.* **154**, 265 (2005).
  - [5] D. Pfannkuche and R. R. Gerhardt, *Phys. Rev. B* **46**, 12606 (1992).
  - [6] C. Albrecht, J. H. Smet, K. von Klitzing, D. Weiss, V. Umansky, and H. Schweizer, *Phys. Rev. Lett.* **86**, 147 (2001).
  - [7] S. Melinte *et al.*, *Phys. Rev. Lett.* **92**, 036802 (2004).
  - [8] C. R. Dean *et al.*, *Nature* **497**, 598 (2013).
  - [9] Y. Cao, V. Fatemi, S. Fang, K. Watanabe, T. Taniguchi, E. Kaxiras, and P. Jarillo-Herrero, *Nature (London)* **556**, 43 (2018).
  - [10] H. Isobe, N. F. Q. Yuan, and L. Fu, *Phys. Rev. X* **8**, 041041 (2018).
  - [11] C. Nayak, *Phys. Rev. B* **62**, 4880 (2000).
  - [12] X. Jia, P. Goswami, and S. Chakravarty, *Phys. Rev. B* **80**, 134503 (2009).
  - [13] D. Hofstadter, *Phys. Rev. B* **14**, 2239 (1976).
  - [14] R. Peierls, *Z. Phys.* **80**, 763 (1933).
  - [15] R. Rammal, *J. Phys. (Paris)* **46**, 1345 (1985).
  - [16] D. J. Thouless, M. Kohmoto, M. P. Nightingale, and M. den Nijs, *Phys. Rev. Lett.* **49**, 405 (1982).
  - [17] G. Naumis, *Phys. Lett. A* **380**, 1772 (2016).
  - [18] G. H. Wannier, *Phys. Status Solidi B* **88**, 757 (1978).
  - [19] Y. Zhang, Y.-W. Tan, H. L. Stormer, and P. Kim, *Nature* **438**, 201 (2005).
  - [20] Y. Hasegawa, Y. Hatsugai, M. Kohmoto, and G. Montambaux, *Phys. Rev. B* **41**, 9174 (1990).
  - [21] F. Evers and A. D. Mirlin, *Rev. Mod. Phys.* **80**, 1355 (2008).
  - [22] J. W. McClure, *Phys. Rev.* **104**, 666 (1956).